Article

3D Heterogeneous Model for Electrodes in Lithium-Ion Batteries and Its Application to a Modified Continuum Model

Mohammadali Mirsalehian [1,*]**, Bahareh Vossoughi** [1]**, Jörg Kaiser** [2] **and Stefan Pischinger** [1,2]

1   Chair of Thermodynamics of Mobile Energy Conversion Systems (TME), RWTH Aachen University, Forckenbeckstraße 4, 52074 Aachen, Germany; bahareh.vossoughi@rwth-aachen.de (B.V.); pischinger_s@tme.rwth-aachen.de (S.P.)
2   FEV Europe GmbH, Neuenhofstraße 181, 52078 Aachen, Germany
*   Correspondence: mirsalehian@tme.rwth-aachen.de

Abstract: The microstructures of porous electrodes in lithium-ion cells strongly affect their electrochemical performance. Experimental tomography techniques to investigate the microstructure during electrode development is costly and time consuming. To address this issue, a numerical method is presented to create a digital morphology to realize a realistic microstructure. In this study, the spherical harmonics in a straightforward mathematical approach are proposed to develop the virtual 3D morphology of the electrode's heterogeneous structure. The introduced method offers a numerically light procedure which enables effective iterative virtual testing and optimization. The generated morphology model is parameterized to reproduce a NMC cathode microstructure observed in the literature. The electrode model allows evaluation of the spatially resolved geometric, transport and electric potential characteristics of the microstructure. The computed characteristics are employed to improve the parametrization of the continuum model as the most widely used physics-based model. For this purpose, the electrochemical impedance spectra of a lithium foil/separator/NMC half-cell is virtually modeled by heterogeneous and continuum approaches. Then, the modified continuum model is compared to the heterogeneous model as a benchmark, in terms of the kinetics and transport characteristics underlying the electrochemical impedance spectra. The modified continuum model shows an improved response in both frequency and time domains.

Keywords: lithium ion batteries; electrode microstructure; spherical harmonics; electrochemical impedance spectroscopy; heterogeneous physical model; modified continuum model

1. Introduction

Lithium-ion batteries (LIBs) with their superior energy and power densities and long lifetime have achieved a dominant role as energy storage system in a variety of applications such as electric vehicles (EVs), consumer electronic devices, energy storage systems and other green industries [1]. Nevertheless, with the industries' demand for further increased energy density, performance and cost savings, optimization studies are, and will still be, required to improve LIBs. Given the time and resources required to develop and characterize new lithium-ion cell types in research labs and at commercial cell manufacturers, computational modeling and simulation offers faster and even more detailed insights on a microscopic level into the processes that are taking place in lithium ion electrodes during charging and discharging. The continuum battery model, developed by the Newman group, is the most widely used physics-based approach to assess the LIB performance [2,3]. Nonetheless, it simplifies the complex electrode microstructure and treats it as a continuum by the aid of approximation methods, e.g., the Bruggeman formulation. The simplification results in a lighter computational effort. However, the existing ambiguities and inadequacies lying in this approach outreach the capability of the continuum model [4–6]. In this work, a fully computer-based approach is presented to model realistic lithium ion electrode

morphologies consisting of active material particles, conducting aids, polymer binders, electrolyte filled pores and current collectors.

The microstructure and the spatial positioning of the constituent domains in LIB electrodes influence the complex interactions between the various underlying electrochemical processes taking place upon LIB operation [7,8]. To gain a comprehensive understanding of the electrode structure and its impact on electrochemical kinetics, it is necessary to reconstruct a virtual morphology of the real heterogeneous electrode structure.

Over the past two decades, the need for modelling realistic particle systems in different fields of science and engineering urged researchers to use material characterization methods such as tomography and 3D laser scanning to obtain the surface information of naturally available or manufactured real particle systems [9]. In recent years, two major modelling approaches to regenerate Li-ion battery electrode microstructures have been employed. On the one hand, experimental tomography techniques such as X-ray Computed Tomography (XCT), Focused-Ion Beam Scanning Electron Microscopy (FIB-SEM), and Transmission Electron Microscopy (TEM), are used either in the initial modelling steps to acquire images of the most realistic particle shapes, which are post-processed via image processing techniques to create a 3D model of the electrode, or as input of realistic physical properties of the battery. Furthermore, this information can be used to validate the obtained model [7,10–21].

On the other hand, the parametric reconstruction of electrode microstructures uses computational or numerical methods to generate shapes as realistic as possible, based on the information of commercially available, manufactured and tested battery cells [22–31].

Obtaining a model from tomography imaging is an expensive and time-consuming process that includes sample destruction which can limit iterative optimization and improvement of the model especially when dealing with prototype electrodes or cells [23,32,33]. Furthermore, the information obtained from imaging techniques might not suffice for battery electrochemistry for multiple reasons. In case of XCT for instance, it is often only the active material (AM) domain structure that is resolved and distinguishing the conductive additives and binder, specifically CBD from the pores, might not be possible [17,34]. Alternatively, the FIB-SEM is not feasible for large electrode samples [8]. The computational modelling approach, however, can provide a conceptual design in the early stages of a research project that allows optimization concerning desired functionality. In other words, virtual material testing and experimenting with various properties of the electrode is possible in short time and little costs [23].

Development of a heterogeneous model allows deep insight into the existing local non-uniformities within the electrode structure to be obtained and hence, uneven localized utilization of active material which can e.g., lead to degradation such as lithium plating on anode material particles [13,35], which are in direct contact or close to the separator interface during fast charging of electric vehicles. Then, the model further enables the optimized battery operating window parameters to be investigated and also aids in advancing the microstructural engineering strategies [4,18,36,37] to alleviate the aging phenomena in the electrode.

Moreover, the electro-chemo-mechanical interactions in an electrode structure can be studied using heterogeneous models. This might include the effect of lithiation and delithiation on development of mechanical strain and stress inside AM particles [38,39], the counter influence of the mechanics on electrochemical performance [40–43] and exploring the possible nucleation and propagation of cracks and delamination in the electrode structure [44–46].

Another application of spatially-resolved modelling could be optimization of the electrode fabrications process including proper mixing and uneven distribution of electrode components during slurry mixing, electrode coating, drying, and calendaring [27,47–49].

In this work, a microstructure model based on numerical computational geometry is developed to virtually represent the complex morphology of the electrode. To generate realistic irregularly shaped particles, the spherical harmonics functions, in a straightfor-

ward mathematical approach, are utilized to define the baseline for the implemented particle shapes. Due to the recent demand on high-energy NMC electrodes, this method is employed to generate a microstructure model representing the irregularities, shapes and orientations existing in real NMC electrodes. The developed electrode model is subsequently analyzed with the Finite Element Method (FEM) to obtain the locally-resolved geometrical and transport properties. It is then assembled with a separator, electrolyte, and lithium foil to compose a Li-foil/separator/NMC half-cell. Hereafter, the electrochemical heterogeneous and continuum models are introduced by a brief illustration of the implemented governing equations which each mathematically describe the physics behind the various electrochemical phenomena in different domains. The continuum EIS model is finally modified to mimic the heterogeneous EIS response using the FEM-based parameters as opposed to the commonly used analytical ways.

2. Methods—Electrode Microstructure

In this section, the computational modelling approach and the construction of the lithium-ion electrode are first described in detail. The model is developed for a NMC cathode case, where the particle dimensions do not change significantly during lithiation and delithiation. The additional effects of particle volume change in a coupled mechanical-electrochemical model will be described soon in another work [50]. In the second part of the section, the FEM-based analysis of the developed electrode is discussed.

2.1. Microstructure Generation

Spherical harmonic expansions have been previously used in various scientific fields, often to solve partial differential equations and to construct mathematical models of physical phenomena. For instance, in quantum mechanics, these functions describe the angular distribution of particles which move in a spherically-symmetric field [51]. In Earth and planetary sciences, the models of the Earth's gravitational field are specially defined by a series of spherical harmonic coefficients (HCs) [52,53]. The models of concurrent magnetic fields, such as the electromagnetism of the Earth's interior, the magnetosphere and in the field of astrophysical studies, are also represented by spherical harmonics [54]. In development of isostatic-topographic models, the global spherical harmonic computation algorithms are employed to evaluate global digital data in acceptable resolutions [55,56]. In another work, the spherical harmonics have been used for the parametrization of the seismic wave phase-speed model [57]. Other applications include calculating and visualizing spatially resolved three-dimensional atomic density profiles around spherically nonsymmetric macro-molecules [58]; investigating the patterns of cell migration that involves dynamic changes in cell shape [59]; or in radiative heat flow models, where the theory of the general elliptic formulation of high-order spherical harmonics methods for arbitrary geometries have been explored [60,61]. In the field of particulate systems, granular structures, and material models such as rocks, sand and powder and their particle mechanics representations, which require generation of irregular-shaped particles, various works have been published that also utilize the spherical harmonics [62–64]. In the field of Li-ion batteries, the generation of realistic virtual microstructures to accurately simulate the electrochemical processes has been the aim of multiple research teams. Feinauer et al., Westhof et al., and Kuchler et al. who have introduced and used stochastic models utilizing the spherical harmonics expansion of Gaussian random fields, have produced distinguished results; more details of this method can be found in [65–68].

Considering the wide range of applications in various multidisciplinary fields of science and technology the spherical harmonics functions have been used in the present work to produce irregular-shaped 3D particles. The bottom-up design approach, modeling each particle individually, is more realistic in comparison to irregular blocks of active material models and allows investigation of local electrochemical (and mechanical) behaviors in neighboring particles. The authors believe that the current algorithm is capable of generating multiple microstructure models simultaneously with different physical properties in a

straightforward mathematical process with lower computational effort in comparison to previous works represented in the literature.

In this algorithm, the definition of the first few real spherical harmonics is directly utilized such that, in each particle, the distance of the surface from the origin (centroid) indicates the absolute value of the function in angular directions (θ, ϕ). To create a realistic particle shape, which is nearly spherical and not perfectly spherical [68], this distance is randomized to deviate the particles from perfect spheres. The analytical solution to derive the function describing the particle surface in the current work is less mathematically complex in comparison to previous stochastic geometry and spatial statistics methods. Hence, it is simpler to recreate the microstructure and investigate the electrochemical behaviors of electrodes in a more realistic FEM model than a homogeneous model with perfectly spherical particles. Furthermore, direct use of a few real spherical harmonics functions allows a faster and easier visualization of the particles in universally used, relatively inexpensive tools such as MATLAB® since the numerical values of spherical harmonics are easily obtainable with the associated Legendre polynomials defined in such tools.

Moreover, COMSOL LiveLink® for MATLAB® is used in the current work to bridge direct mesh data transfer from MATLAB® to COMSOL Multiphysics® software to create the FEM model, which has also contributed to the increase in speed of preparing large models with hundreds of individually created particle mesh files.

The following includes a review of spherical harmonics functions and a description of the introduced algorithm.

2.1.1. Spherical Harmonics

Spherical harmonics are a set of functions used to represent spherical functions. A spherical function, defined on the surface of a sphere S^2, is a mapping of spherical coordinates (r, θ, φ) to a scalar value.

Spherical harmonics arise in the solution to Laplace's equation, which imposes that the Laplacian of a scalar field f is zero. These functions are constructed as eigenfunctions of the angular part of the Laplacian in three dimensions [69]. This construction is analogous to the case of the trigonometric functions $\sin(m\varphi)$ and $\cos(m\varphi)$, which form a complete basis for periodic functions of a single variable (functions on the circle S^1), and are the eigenfunctions of the angular Laplacian in two dimensions, $\nabla^2 \varphi = \frac{\partial^2}{\partial \varphi^2}$, with eigenvalue $-m^2$. In other words, the spherical harmonics are a higher-dimensional analogy of the Fourier series.

The Laplace equation $\nabla^2 f = 0$ in spherical coordinate system,

$$\nabla^2 f = \frac{1}{r^2} \frac{\partial}{\partial r} \left(r^2 \frac{\partial f}{\partial r} \right) + \frac{1}{r^2 \sin \theta} \frac{\partial}{\partial \theta} \left(\sin \theta \frac{\partial f}{\partial \theta} \right) + \frac{1}{r^2 \sin^2 \theta} \frac{\partial^2 f}{\partial \varphi^2} = 0, \tag{1}$$

can be solved by separation of variables. The solutions are of the form $f(r, \theta, \varphi) = R(r)Y(\theta, \varphi)$ and the following two differential equations are obtained for the radial and angular parts of the solution:

$$\frac{1}{R} \frac{d}{dr} \left(r^2 \frac{dR}{dr} \right) = \lambda, \tag{2}$$

$$\frac{1}{Y} \frac{1}{\sin \theta} \frac{\partial}{\partial \theta} \left(\sin \theta \frac{\partial Y}{\partial \theta} \right) + \frac{1}{Y} \frac{1}{\sin^2 \theta} \frac{\partial^2 Y}{\partial \varphi^2} = -\lambda. \tag{3}$$

Applying separation of variables to the second PDE, the angular equation, the solution will be of the form $Y(\theta, \varphi) = \Theta(\theta)\Phi(\varphi)$. The azimuth angle dependent solution will be in form of the trigonometric functions $\sin(m\varphi)$ and $\cos(m\varphi)$ or $e^{\pm im\varphi}$ for $m \geq 0$.

Furthermore, the polar-angle-dependent solution is the general Legendre equation considering $\lambda = l(l+1)$ where $l \geq 0$ and $|m| \leq l$, with the reparametrization in terms of angles $x = \cos\theta$ and using the relation $1 - x^2 = \sin^2\theta$:

$$\left(1 - x^2\right) \frac{d^2}{dx^2} P_l^m(x) - 2x \frac{d}{dx} P_l^m(x) + \left[l(l+1) - \frac{m^2}{1 - x^2}\right] P_l^m(x) = 0. \tag{4}$$

The associated Legendre polynomials $P_l^m(x)$, with the degree l and order m (both integers), are the canonical solutions of the general Legendre equation.

Combining both the trigonometric functions and the associated Legendre polynomials $P_l^m(\cos\theta)$, the general solutions for each linearly independent $Y(\theta, \varphi)$, the angular solution of the $\nabla^2 f = 0$, can be written as

$$Y_l^m(\theta, \varphi) = \sqrt{\frac{2l + 1}{4\pi} \frac{(l - m)!}{(l + m)!}} e^{im\varphi} P_l^m(\cos\theta). \tag{5}$$

$Y_l^m(\theta, \varphi)$ are the spherical harmonic functions of degree l and order m, with a normalization constant (the expression under square root) multiplying the solution to make independent spherical harmonics orthonormal.

Any spherical function can be visualized by displaying the points on the surface of the sphere along its corresponding normal vector based on the value of the function. This has been the method to generate irregular shaped particle mesh varying from spheres and ellipsoids to represent the active material particles of the LIB electrode microstructure.

In the current manuscript, the spherical function defined to generate 3D irregular-shaped particles, is assumed to have a real value. However spherical functions with a complex value can also be harmonically expanded by the complex spherical harmonics as well. Moreover, due to the randomized input parameters of the algorithm, the positive or negative extension of the spherical harmonic functions are considered ineffective in the final model. Hence, degrees and orders of the spherical harmonics are assumed to be positive integers ($0 \leq m \leq n$).

2.1.2. Active Material Domain

To generate irregular shaped and randomly distributed particles, a MATLAB® algorithm has been developed utilizing the Gaussian normal distribution and the associated Legendre polynomials.

The normal distribution is often referred to as $N(\mu, \sigma^2)$ where μ is the mean of the distribution, the parameter σ is its standard deviation and σ^2 is defined as the variance of the distribution. When a random variable Z is normally distributed with mean μ and standard deviation σ, it may be written $Z \sim N(\mu, \sigma^2)$. The standard normal distribution is defined as a normal distribution with a mean of zero and a standard deviation of 1: $N(0, 1)$.

The values of the following function, Equation (6), define the points on the surface of an irregular spherical shape with unit radius

$$Y_{Z_1, Z_2}(\theta, \varphi) = \left(Z_1 P_l^m(\cos\theta) + Z_2 P_l^m(\cos 2\theta)\right) \cos m\varphi \tag{6}$$

in which P_l^m are the associated Legendre polynomials with $m = l - 1$, and $Z_1, Z_2 \sim N(0, 1)$ are any randomly generated scalars drawn from the standard normal distribution.

To control the irregularity of the surface, a parameter A is defined as noise amplitude. The amplitude is then used alongside the randomized actual particle radius r, that is calculated based on the realistic average NMC AM particle radius r_p derived from literature, $r \sim N(r_p, \sigma^2)$, to calculate the distance of each point of Y from the centroid of the particle with Equation (7):

$$\rho = r + \frac{AY}{\max|Y|}. \tag{7}$$

To randomly deviate the particle shapes from spherical to ellipsoidal, the two randomly generated scalar parameters a and b are defined as $a \sim N(1.1, 0.04)$ and $b \sim N(1.1, 0.04)$.

Finally, in order to generate the meshes, the spherical coordinates are mapped to the Cartesian system with the following equations:

$$x = a\rho \sin\theta \cos\varphi, \tag{8}$$

$$y = b\rho \sin\theta \sin\varphi, \tag{9}$$

$$z = \rho \cos\theta. \tag{10}$$

For given NMC electrode microstructure dimensions and desired AM domain volumetric content, a loop generates the surface meshes until the total target volume is reached.

In the next step, the particle centroid coordinates are calculated based on the particle radii and the optimal distances of the neighboring particle centroids. To finalize the electrode model mesh, hundreds of particles have been imported in COMSOL Multiphysics® via an algorithm written in COMSOL LiveLink® for MATLAB®.

The main characteristics of a realistic NMC electrode and its geometrical information have been extracted from references such as [7,16,21], which also include SEM images of NMC microstructure and particle size distribution. The characteristics are then translated into the required parameters for the developed algorithm to construct the virtual morphology. Observing [16,21], it is considered to construct the NMC particles from a spherical core with mean radii of 2 µm and 5 µm. The size distribution of NMC particles across electrodes varies in different studies, however, a normal distribution is a common one and it is shown that a normal distribution of average particle diameter in the RVE is comparable to the tomography data [7]. The initial sphere sizes have been randomized with two normal distributions each about the mean radii 2 µm and 5 µm with a standard deviation of 0.2 µm. Further measures (the calculated scalar parameters Z_1, Z_2, a, b, and amplitude noise A) as explained in the algorithm, are taken to deviate the shapes from perfect spheres, resulting in a unimodal particle size distribution with shifted mean value. The final size distribution of the irregular shaped particles inside the modeled electrode is plotted in the Figure 1. Different stages to generate the final model of the cathode microstructure are shown in Figure 2.
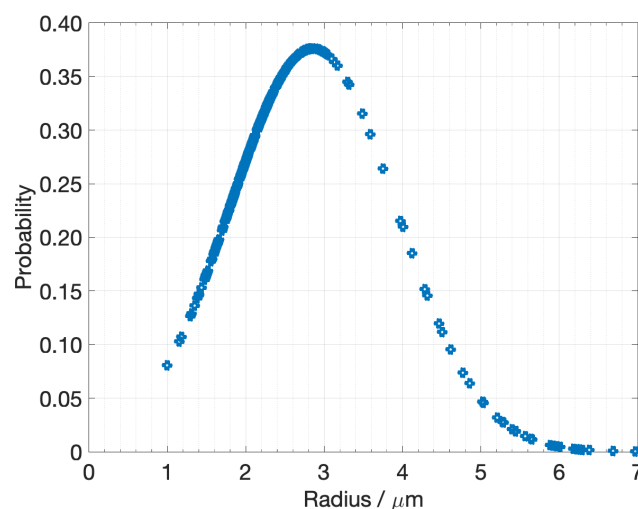
Figure 1. Final irregular shaped particle size distribution inside the electrode microstructure model used in this work.
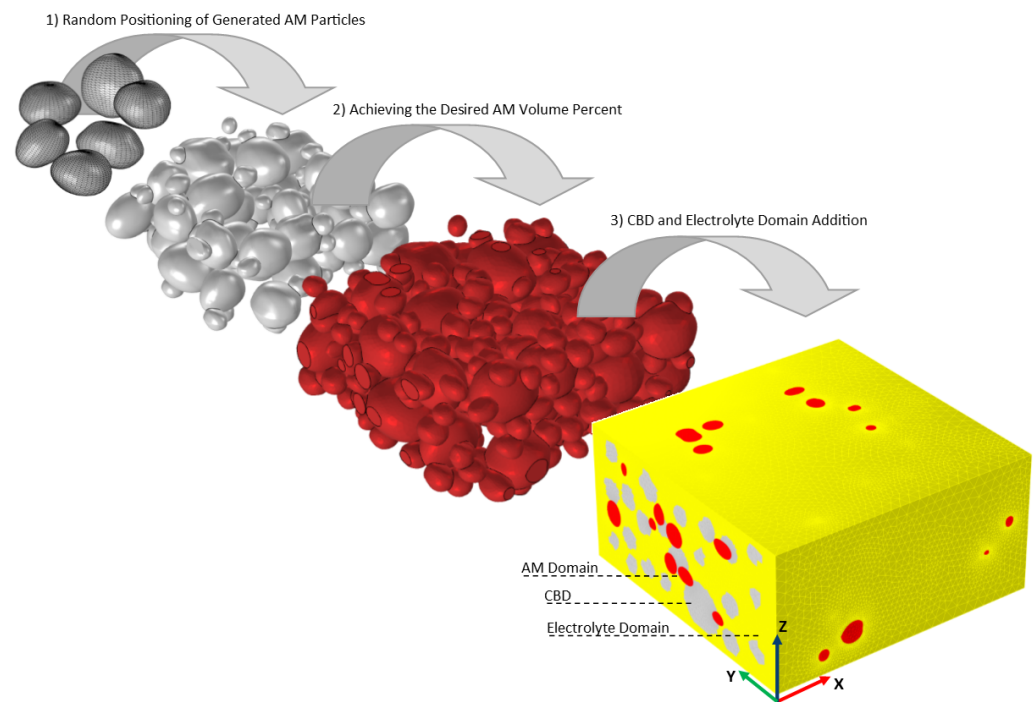
Figure 2. Cathode microstructure generation process. (1) Generated AM particles are positioned randomly, this process is continued until (2) the desired volume percent is reached, (3) CBD and electrolyte domains are added to the electrode. In addition, the electrochemical cell used in this work includes a 6.5 μm Al foil in the yz-plane at $x = 50$ μm serving as an electric current collector, while at $x = 0$ μm an electrolyte filled separator domain of 11 μm thickness followed by lithium foil as a counter electrode are placed (see Table 1).

Table 1. Half-cell RVE microstructure generation specifications.

Property	Value
Cathode microstructure dimension	$50 \times 50 \times 25$ μm^3
Average NMC particle radius r_p	2 μm and 5 μm
Radius standard deviation	0.2 μm
Active material volumetric fraction	49.6%
Carbon binder domain volumetric fraction	4.6%, 7%, 10%, 12.5%
Porosity	45.8%, 43.4%, 40.4%, 37.9%
Separator thickness	11 μm
Al current collector thickness	6.5 μm

2.1.3. Carbon Binder Domain

To improve the low electric conductivity of the active material particle layers, a conductive agent is added in small quantities. In addition, a polymer strengthens the mechanical integrity of the electrode structure by bonding active material particles to each other and to the supporting current collector (CC) foil. To account for their influence on electrode performance, it is necessary to include the virtual morphology of CBD in the model as well. However, as mentioned earlier, spatially resolving CBD in the electrode is challenging by imaging methods. Therefore, Hein et al. [16] studied different distributions of CBD and indicated that only a very dense CBD which resides at the contact points of particles is able to reproduce the measurement data. In such morphology, CBD forms a bridge between the neighboring AM particles.

In this work, using spatial shape functions and randomly positioning, the remaining space between AM particles inside electrode is partially filled. The size of CBD has been chosen in a range which functions as connecting bridges between particles. The resulting CBD is sliced up by the already-generated heterogeneous particles in the electrode and con-

sequently, spatial porous regions of different sizes and shape form carbon-binder domain. Following generating the CBD regions, the AM particles are partially covered providing limited sites for the electrochemical reactions, similar to a real electrode. Furthermore, the random positioning of the CBD within the electrode microstructure might result in isolated AM particles which do not contribute electrochemically as observed in the reality. To investigate the effects of CBD content on electrode behavior, four models with different volume contents of 4.6%, 7%, 10%, and 12.5% are developed.

Finally, a half-cell RVE (Representative Volume Element) is developed by assembling the generated electrode microstructure, explained before, with two cubic domains and a boundary to represent the separator domain, the current collector domain and the lithium foil. The properties considered to generate the currently developed half-cell RVE are listed in Table 1. The length of 25 µm of the short RVE edge in relation to the mean particle radius of 2.85 µm gives a L/d ratio of 4.39. According to Chen et al. [70] a minimum ratio of 2.5 is sufficient to regard an RVE as a statistically representative sample.

2.2. FEM-Based Calculation of the Effective Transport Coefficients of the Developed Electrode

The LIB continuum model treats the porous electrode as a macro-homogeneous and isotropic medium. In this modelling approach, the effective transport characteristics of the porous electrode are calculated using two dimensionless parameters defined on the electrode level, porosity ϵ, and tortuosity factor τ. This is performed by using the MacMullin number (N_M), Equation (11), and application of the widely used Bruggeman approximation Equation (12), which correlates the tortuosity factor of porous media to their porosity:

$$N_M = \frac{\tau}{\epsilon} = \frac{\alpha_{\text{bulk}}}{\alpha_{\text{eff}}}, \tag{11}$$

$$\tau = \epsilon^{-0.5} \tag{12}$$

where α_{bulk} and α_{eff} represent the bulk and effective transport coefficients, respectively. Although the Bruggeman formulation provides a straightforward analytical way to predict the effective transport coefficient within porous electrodes, it cannot be employed for electrodes with morphological complexities since it does not account for the electrode morphology dependency. Moreover, the anisotropic nature of transport in a porous electrode is not captured by using this formulation.

To address these issues, an FEM-based method is applied to compute the effective transport coefficients of the developed electrode microstructure and its tortuosity factor. For this purpose, the steady-state continuity Equation (13) and a stream flux Equation (14), which is driven by a dimensionless potential field gradient, are implemented in the pore domain Γ_{pore}.

$$\iiint_{\Gamma_{\text{pore}}} -\text{div}\vec{j}\,dV = 0, \tag{13}$$

$$\vec{j} = -\alpha_{\text{bulk}}\vec{\nabla}\phi. \tag{14}$$

Equations (13) and (14) analogously describe the transport mechanisms of diffusion and migration, ϕ being the dimensionless potential field and α_{bulk} its respective bulk transport coefficient in [m²/s] resulting in stream flux $\vec{j}$ in [m/s]. Two Dirichlet boundary conditions of $\phi = 1$ and $\phi = 0$ are set on the inlet and outlet boundaries to account for the potential gradient across the pore domain. Given $x = L_{electrode}$ representing the electrode thickness, the illustrated boundary conditions

$$\phi = 1, \quad \partial\Gamma_{\text{inlet}} = \{(x,y,z) \in \Gamma_{\text{pore}} : x = 0\},$$
$$\phi = 0, \quad \partial\Gamma_{\text{outlet}} = \{(x,y,z) \in \Gamma_{\text{pore}} : x = L_{\text{electrode}}\}.$$

are used to analyze electrolyte transport across the electrode thickness (x). For the other two dimensions of y and z, similarly, the relevant inlet and outlet boundaries, $\partial\Gamma_{\text{inlet}}$ and $\partial\Gamma_{\text{outlet}}$, are accordingly chosen to generate the potential gradient in the desired direction.

The calculated potential field and flux stream within the pore domain are then further utilized and substituted into Equations (15) and (16) to calculate the effective transport coefficient across the electrode thickness (x).

$$\overline{\phi}(x) = \frac{\iint_{\partial\Gamma_{\text{interface}}} \phi \, dy \, dz}{\iint_{\partial\Gamma_{\text{interface}}} dy \, dz} \tag{15}$$

$$\alpha_{\text{eff}}(x) = \frac{\iint_{\partial\Gamma_{\text{interface}}} -\alpha_{\text{bulk}}\left(\frac{\partial\phi}{\partial x}\right) dy \, dz}{S_{\text{electrode}} \cdot -\frac{\partial\overline{\phi}}{\partial x}|_{\partial\Gamma_{\text{interface}}}} \tag{16}$$

$$\partial\Gamma_{\text{interface}} = \{(x, y, z) \in \Gamma_{\text{pore}} : 0 < x < L_{\text{electrode}}\}$$

While $\overline{\phi}$ is the averaged potential field across the electrode thickness, $S_{\text{electrode}}$ is the total electrode cross section.

The electronic effective transport coefficient of the electrode microstructure is similarly calculated in the solid regions of CBD and AM domain. Since the electronic conductivity of the CBD and AM particles are significantly different, Equation (16) is reformulated to assign combined transport behavior of CBD and AM domain to the total electrode.

3. Methods—Electrochemical Model

3.1. Governing Equations

Both a heterogeneous 3D model and a continuum model are developed to represent the lithium-foil/separator/NMC electrode cell. The physics employed to describe various coupled electrochemical interactions in different domains and the cell parameters and constants utilized in the models are provided in Tables 2 and 3. In the equations, the subscripts s and e denote solid and electrolyte phase properties, respectively. Here is a brief description of the physical processes considered in each domain.

Table 2. List of physics implemented in different domains in the half-cell.

Domain/Boundary	Equation
AM, CBD, CC	$\vec{\nabla}.(\sigma_s \vec{\nabla}_{\phi_s}) - j^{\text{total}^*} = 0$
AM	$\frac{\partial c_s}{\partial t} + \vec{\nabla}.(-D_s \vec{\nabla} c_s) = 0$
Pore, separator	$\frac{\partial(\varepsilon_e^{**} c_e)}{\partial t} = \vec{\nabla}.D_e^{\text{eff}} \vec{\nabla} c_e + \frac{1-t_{\pm}^0}{F} j^{\text{total}^*}$
	$\vec{\nabla}.(\kappa^{\text{eff}} \vec{\nabla} \phi_e) + \vec{\nabla}.(\kappa_D^{\text{eff}} \vec{\nabla} \ln(c_e)) + j^{\text{total}^*} = 0$
Pore (continuum model), Separator	$D_e^{\text{eff}} = (\varepsilon_e)^p \cdot D_e^{\text{bulk}}$
	$\kappa_e^{\text{eff}} = (\varepsilon_e)^p \cdot \kappa_e^{\text{bulk}}$
AM-electrolyte interface	$j^f = A_v \cdot j_0 \left(\exp\left(\frac{\alpha_a F \eta}{RT}\right) - \exp\left(-\frac{\alpha_c F \eta}{RT}\right) \right)$
	$j_0 = F k c_s^{\alpha_c} (c_{s,\text{max}} - c_s)^{\alpha_a} \left(\frac{c_e}{c_{e,\text{ref}}}\right)^{\alpha_a}$
	$\eta = \phi_s - \phi_e - U$
	$j^c = A_v \cdot \frac{\partial(\phi_s - \phi_e)}{\partial t} \cdot C_{\text{DL}}$
	$j^{\text{total}} = j^f + j^c$

* $j^{\text{total}} = 0$ in CBD, CC and separator domains. ** ε_e excluded in equation for pore domain in heterogeneous model.

Table 3. Parametrization of the models of the half-cell.

Parameters	Value	Ref.
NMC Particles		
AM solid conductivity (σ_s)	0.17 S/m	[71]
AM solid diffusivity (D_s)	$1 \cdot 10^{-14}$ m^2/s	[72]
max AM solid concentration ($c_{s,\max}$)	49,000 mol/m^3	[73]
Equilibrium potential (U)	$-180.7 \cdot SoL^7 + 572.0 \cdot SoL^6 - 722.3 \cdot SoL^5 + 463.8 \cdot SoL^4 - 160.4 \cdot SoL^3 + 29.9 \cdot SoL^2 - 3.9 \cdot SoL + 4.4$ V	[73]
Kinetics		
Reaction rate constant (k)	$7.645 \cdot 10^{-10}$ m/s	[74]
Transfer coefficients (α_a, α_c)	0.5	
Surface double layer capacitance (C_{DL})	0.2 F/m^2	[74]
Bruggeman exponent (p^*)	1.5	
Current collector		
Conductivity (σ_s)	$3.7 \cdot 10^7$ S/m	[71]
Carbon binder domain		
Conductivity (σ_s)	100 S/m	[4]
Electrolyte		
Electrolyte reference concentration ($c_{e,\mathrm{ref}}$)	1000 mol/m^3	[71]
Conductivity (κ_e)	$0.32 \cdot (c_e/c_{e,\mathrm{ref}})^3 - 1.6 \cdot (c_e/c_{e,\mathrm{ref}})^2 + 2.2 \cdot (c_e/c_{e,\mathrm{ref}}) + 0.03$ S/m	[75]
Diffusivity (D_e)	$0.04 \cdot (c_e/c_{e,\mathrm{ref}})^3 - 0.24 \cdot (c_e/c_{e,\mathrm{ref}})^2 + 0.24 \cdot (c_e/c_{e,\mathrm{ref}}) + 0.31 \cdot 10^{-9}$ m^2/s	[75]
Activity ($\partial \ln f / \partial \ln c_e$)	$-0.43 \cdot (c_e/c_{e,\mathrm{ref}})^3 - 1.5 \cdot (c_e/c_{e,\mathrm{ref}})^2 - 0.08 \cdot (c_e/c_{e,\mathrm{ref}}) - 0.014$	[75]
Transference (t_+^0)	$-0.17 \cdot (c_e/c_{e,\mathrm{ref}})^4 + 0.6 \cdot (c_e/c_{e,\mathrm{ref}})^3 - 0.6 \cdot (c_e/c_{e,\mathrm{ref}})^2 + 0.08 \cdot (c_e/c_{e,\mathrm{ref}}) + 0.3$	[76]

* for continuum model, modified exponent (p^m) is used.

3.1.1. Solid Domains

Ohm's law is implemented in AM, CBD and CC domains which are electronically conductive. To simplify the model, no electronic contact resistance between these domains is considered. The CBD is assumed to be impermeable to lithium ions and therefore, the ion normal flux on CBD boundaries are set to zero. The same boundary condition is assigned also to the CC boundaries.

At AM-electrolyte interfaces, the electrochemical reaction kinetics, the volumetric faradaic current density j^f, is described by the Butler–Volmer equation. Moreover, to account for the double layer (DL) formed at this interface, a homogeneous volumetric capacitive current density j^c is added to the faradaic current density to compose the total volumetric current density j^{total} at these interfaces.

To describe solid-state diffusion, the ideal solution theory is employed, and the formulation of Fick's second law is implemented in the AM domain. Then, the Neumann boundary condition is set at the AM-electrolyte interface to account for the coupled physics of the faradaic current density and the diffusion inside the AM particles.

3.1.2. Pore and Separator Domains

It is assumed that the pore domain, which is in between solid domains, is fully filled with the liquid electrolyte. The separator domain is assumed as a porous electrolyte-permeable media with 50% of its volume accessible to the electrolyte.

To simplify the model and account for the separator's porous nature, the Bruggeman relation is utilized to predict the effective transport coefficients of the separator domain.

The electrolyte transport is mathematically described in accordance with the concentrated solution theory. The transport equations are slightly reformulated to consider the porous nature of the separator which is not explicitly included in the developed microstructure of separator domain.

3.1.3. Lithium Foil Boundary

The lithium foil is represented as a boundary and the volumetric current density of lithium metal deposition and dissolution that occurs at the interface between the lithium foil and the electrolyte is mathematically described by the Butler–Volmer equation with zero overpotential in order to not introduce additional impedance. This means, that the calculated impedances consist of contributions from the porous separator and cathode microstructure (both filled with electrolyte) with a current collector foil attached.

3.2. Electrochemical Impedance Spectroscopy

Electrochemical Impedance Spectroscopy (EIS) is a powerful non-destructive tool to characterize electrochemical systems. EIS modelling allows the underlying physics behind the cell performance to be de-convolved. Several studies have been conducted on development of the EIS models using a so called Transmission Line Model (TLM). In spite of the efforts made by the authors to consider variant distributions of pore sizes inside the electrode microstructure in TLMs [77–80], there is an intrinsic drawback of simplifying the complex electrode microstructure into arbitrary morphologies and not considering the constituent domains. Therefore, recently some authors have reported development of EIS models based on heterogeneous approaches, which include the electrode composition and the physics that describe the respective phenomena in each domain [1,16,81,82]. Such an EIS model can be hired to modify the commonly used continuum model, using the developed heterogeneous model as the benchmark. Although there are few studies which aimed at evaluation and modification of the continuum model in terms of different sources of overpotentials [4,25,36] and spatially resolved geometrical parameters [83] , the quantitative evaluation of introduced modifications has not been carried out in frequency domain based on electrochemical impedance spectra which provides a high resolution assessment.

The transient electrochemical response of an electrolyte-filled porous electrode is composed of different rate-limited coupled interactions which occur on different time and length scales within the microstructure. Each of these coupled interactions contributes to the electrode impedance spectra signature. Since their contributions vary on diverse timescales, numerical modeling allows for the deconvolution of the underlying interactions that determine the total electrode electrochemical impedance.

The electrochemical interactions exhibit not only timescale dependency, but also take place on different length scales. Ionic and electronic transports are realized on the electrode scale within the electrolyte, the AM, and the CBD domains. The transport limitation within these domains arises from finite bulk transport coefficients and, moreover, the porous nature of the electrode morphology further hinders the transport characteristics. On the other hand, the lithium intercalation process takes place on the particle scale and it is kinetically limited by the interfacial impedance. Lithium intercalation encompasses two distinguished coupled processes; electrochemical reaction at the AM-electrolyte interface, and lithium solid diffusion inside the AM particles. These two processes form the faradaic component of interfacial impedance. Furthermore, the developed electrochemical double layer (DL) in the confined region in the vicinity of electrode-electrolyte interface originates the capacitive component of the interfacial impedance. In porous electrodes, the formed DL across the electrode-electrolyte interface throughout the whole electrode structure impacts the electrochemical response dynamics of the electrode. The latter capacitive component in conjunction with the former faradaic behavior modulates the interfacial impedance on the particle scale.

The governing equations in Table 2 express the electrochemical response in the time domain. Therefore, to gain the electrochemical impedance, the equations are transformed to

the frequency domain using the Laplace transformation. For this purpose, the equations are initially linearized around an equilibrium state, similar to an EIS measurement conducted on a resting and equilibrated cell. In addition, a harmonically oscillating voltage signal with varying frequency and small magnitude, is applied to perturb the half-cell. The voltage input signal magnitude is set to a sufficiently small value of 10 mV to ensure a linear electrochemical response of the half-cell. The input signal frequency is varied from 1 mHz to 100 kHz.

The simulations are carried out in COMSOL Multiphysics® 6.0 using an Intel® Xeon® CPU @ 3.70 GHz (2 processors) with 128 GB of RAM.

4. Results and Discussion

### 4.1. Numeric-Based Analysis of Electrode Porous Microstructure

Electrode morphology determines the effective properties of the whole porous microstructure and contributes to the total impedance of the electrode. This includes the volume fraction of each component, shapes and locations of them in relation with each other that correlate directly with the electrode performance.

To geometrically analyze the microstructure, sequential volume and surface integrals over the relevant domains are calculated to obtain the main characteristics of the developed electrode model. Figure 3 shows the calculated geometrical features of the reconstructed electrode 3D microstructures with different CBD volume fractions as a function of the normalized length (X) in the electrode thickness direction of the electrode. In brief, $X = 0$ and $X = 1$ represent the cathode–separator and cathode–current collector interfaces, respectively. Figure 3a depicts the AM particle volume fraction ε_{AM} across the electrode which is not varied in the different investigated cases. However, the porosity ε_e alters when changing the CBD content ε_{CBD} as depicted in Figure 3b,c. More CBD content results in larger used-up regions in the pore domain and decreased porosity of the electrode. Figure 3d demonstrates the evolution of the specific active surface area A_v which is exposed to the electrolyte. Presence of CBD results in partial blocking of the active particle–electrolyte interface meaning less area for the electrochemical reaction since the carbon-binder domain is impermeable to Li^+ ions. Therefore, as observed in Figure 3d, more CBD content leads to less available active surface area in the electrode microstructure. The FEM-calculated specific surface area is also compared with widely used analytical formula, $A_v = 3\varepsilon_e/\bar{r}_p$, which is driven based on a non-complex porous media containing simple spherical particles of the same size. As can be observed, the prediction by the formula is not able to capture the influence of the existing irregularities and the obstruction caused by the CBD in the electrode.

In this study, the effective transport properties in the pore and solid domains in the electrode microstructure are calculated using FEM and compared to the widely used Bruggeman correlation. In this regard, Figure 4a,b depict the iso-surfaces of the calculated potential field ϕ and its resulting stream flux $\vec{j}$ in the pore domain. The FEM-based calculated fraction of the effective transport property to its respective bulk value $\alpha_e^{\text{effective}}/\alpha_e^{\text{bulk}}$ is computed for different CBD contents and directions and compared with the values predicted by the Bruggeman correlation in Figure 4c–f. As can be seen, the value calculated by the FEM differs from the Bruggeman-predicted value because the formula is independent of the electrode composition. For example, more porous regions on the sides of electrode microstructure results in higher effective transport property which is reflected in the FEM calculation and, on the opposite side, the Bruggeman formula is average-based and independent of the composition. Furthermore, the FEM enables the effective transport property in different directions to be obtained, while the analytical formula does not consider transport anisotropy in the electrode porous structure, which implies another capability of the FEM calculation over the Bruggeman method.
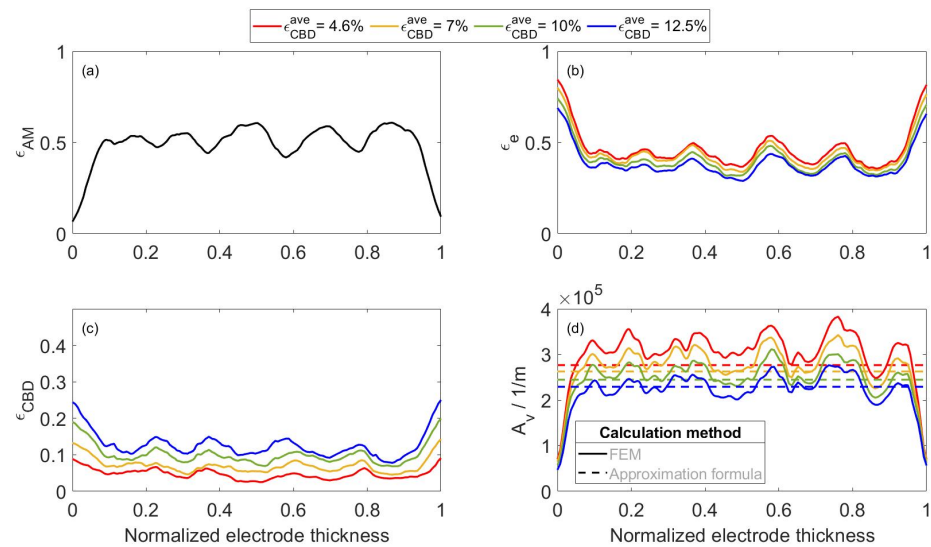
Figure 3. Geometrical characteristics of reconstructed electrode microstructure including volumetric fraction of AM domain (**a**), pore domain (**b**), CBD (**c**) and specific active surface area (**d**).
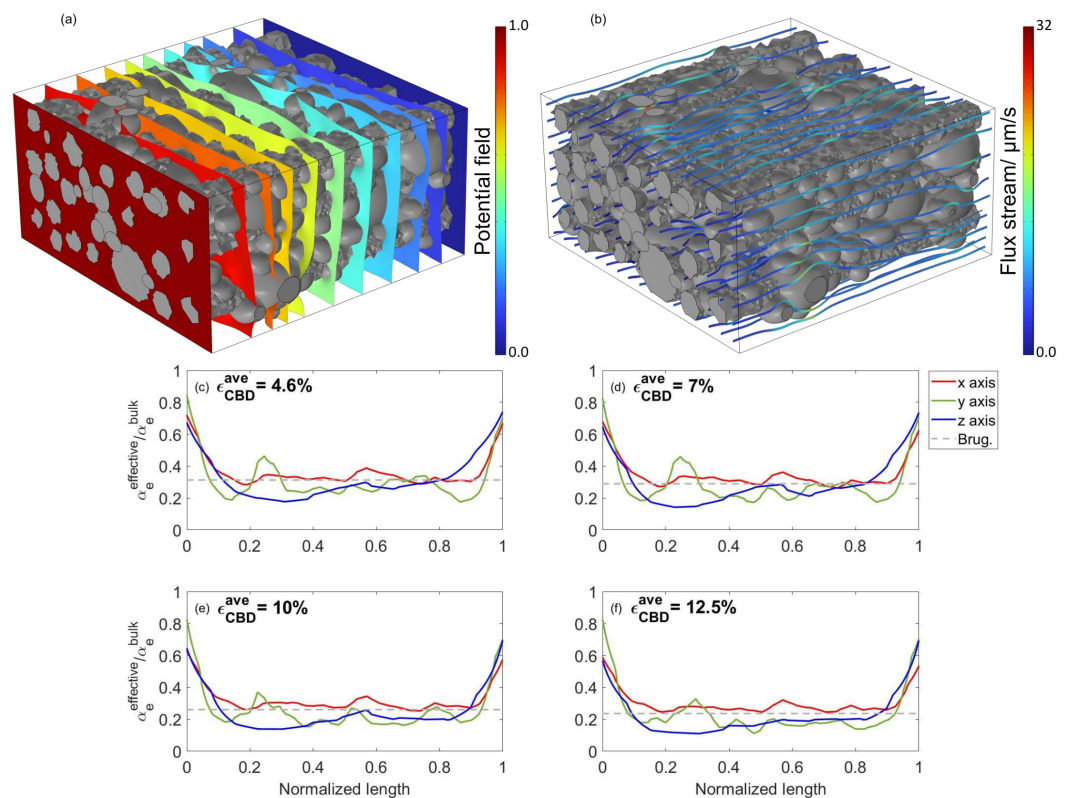

Figure 4. Iso-surfaces of potential (**a**) and resulting stream flux (**b**) across pore domain under potentiostatic conditions. FEM-based directional $\alpha_e^{eff}/\alpha_e^{bulk}$ in different CBD contents and the obtained counter value by the Bruggeman formula (**c**–**f**).

The spatially resolved porosity and the FEM-calculated local effective transport property of the electrode structure in different directions are used to obtain the local and directional tortuosity factor τ using the MacMullin number. The acquired tortuosity factor is further utilized to attain the modified exponent p^m to adjust the Bruggeman formula. Figure 5 illustrates the FEM-based directional tortuosity factors and the modified exponents for different CBD contents and compares to their respective Bruggeman-predicted values. The tortuosity factor, which represents the obstruction to free-space caused by complex

pathway [12], is spatially resolved by the FEM calculation, and the evolution of the solid obstacles across the electrode length in different directions is captured which is in contrast to the Bruggeman estimation. The analysis of our electrode microstructure yields tortuosity values from 1.1 to 2.7 (Figure 5a,c,e,g), where the local maxima and minima depict less porous and more porous regions respectively in the structure. For the sake of better readability, the x-axis in Figure 5 is given in absolute length of the electrode in different directions instead of normalized length. Considering an averaged tortuosity value of 1.9 which is obtained in this work, Landesfeind et al. [84] reported a ∼7% lower tortuosity value of 1.77 for an NMC electrode with a similar porosity, derived from a numeric method using a 3D reconstruction of the electrode based on X-ray tomography whereas a tortuosity value of 3.1 derived from EIS experiments on the same electrode. The discrepancy between the tortuosities obtained by the numeric method and EIS experiment is attributed to the assumption that is made to attain the tortuosity through experiments. In EIS method, by assuming a negligible electronic resistance in the solid phase of the porous electrode, the measured total impedance spectrum is solely assigned to the ionic resistance enabling to derive the tortuosity. While such an assumption for electronically well-conductive electrodes, for instance graphite, is reasonable, an NMC cathode with low electronic conductivity results in an error. Figure 5b,d,f,h demonstrate the modified exponent p^m in different directions and CBD contents, in contrast to the Bruggeman exponent ($p = 1.5$), providing a reasonable indicator of the existing insufficiency of the Bruggeman formula.
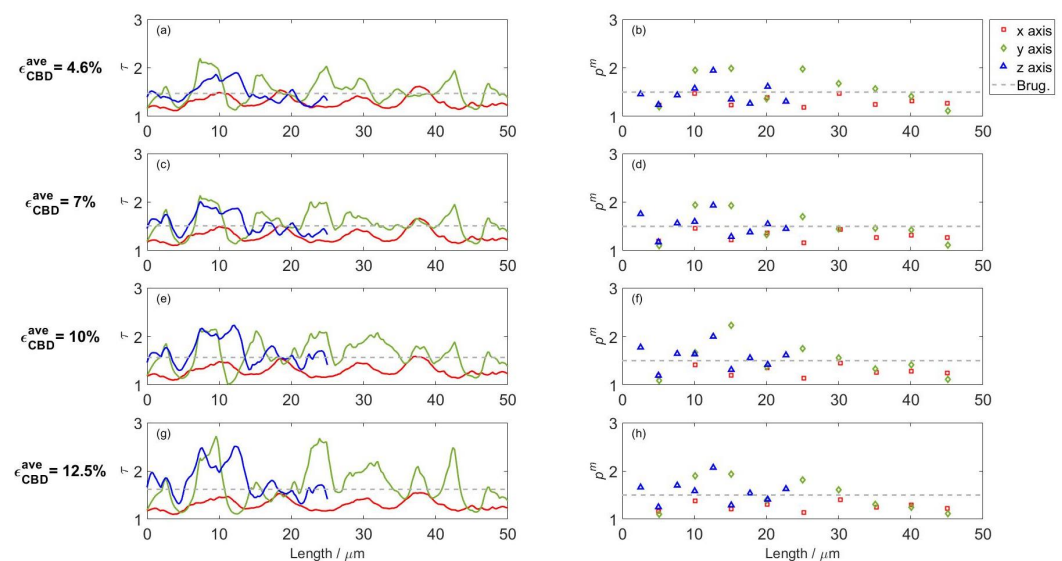
Figure 5. Directional tortuosity factor τ (**a**,**c**,**e**,**g**) and modified exponent p^m (**b**,**d**,**f**,**h**) in different CBD contents as opposed to the Bruggeman counter values.

Similarly, the effective electronic transport property of the solid regions composed of AM and carbon-binder domains in the electrode thickness direction is obtained by the FEM and compared to the Bruggeman-predicted values. Figure 6a,b show the iso-surfaces of the calculated potential field ϕ and its resulting stream flux $\vec{j}$ in the solid domains composed of non-highly conductive NMC particles and highly conductive CBD regions. Figures 4b and 6b indicate the significantly higher electronic transport characteristics in solid domains as compared to ionic transport characteristics in the electrolyte. As observed in Figure 6c, presence of the CBD in the electrode microstructure improves the effective electronic conductivity of the electrode by an order of magnitude compared to a pure NMC electrode, in spite of low volumetric content of the CBD. Furthermore, Figure 6c also implies that the conductivity across the electrode thickness strongly relies on the spatial fraction of the volumetric content of CBD over AM content. Since the fraction alters continuously across the electrode, such fluctuating conductivity is acquired, which cannot be implicated by the Bruggeman correlation.
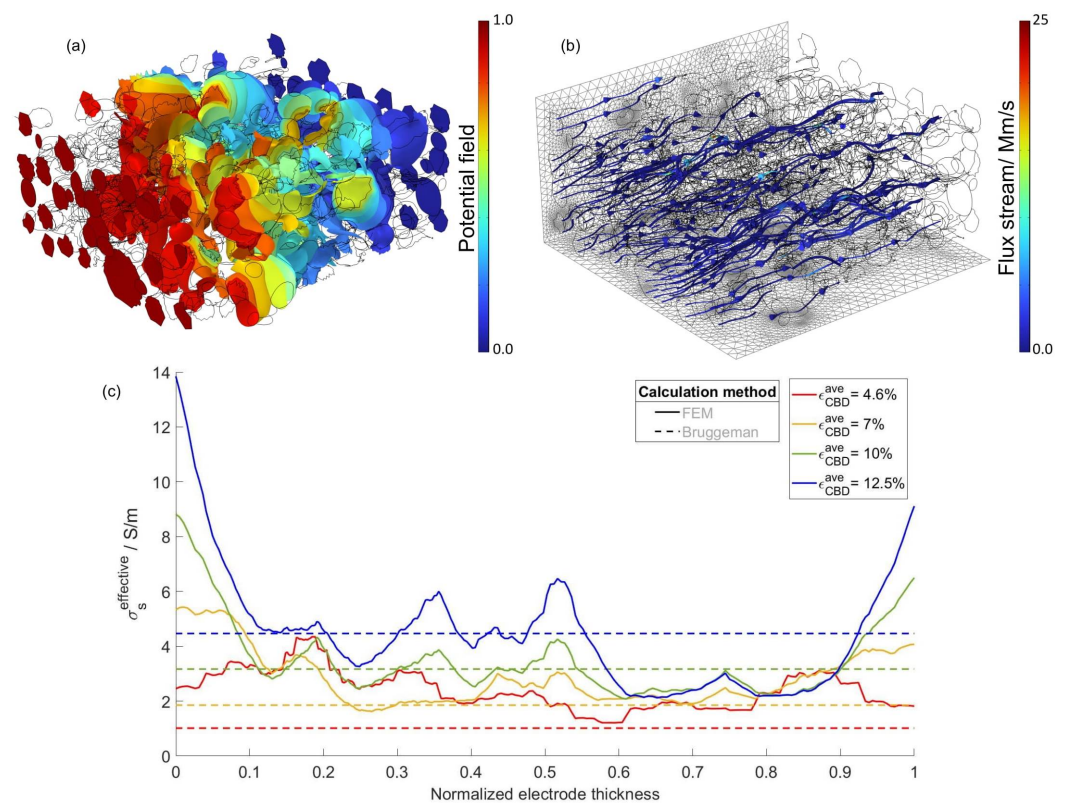
Figure 6. Iso-surfaces of potential (**a**) and resulting stream flux (**b**) across AM and carbon-binder domains under potentiostatic conditions. FEM-based σ_s^{eff} in electrode thickness direction by different CBD contents and the obtained counter value by the Bruggeman formula (**c**).

4.2. Numeric-Based Impedance Spectra

Figure 7 illustrates the computed impedance spectra by the heterogeneous model which allows the investigation of morphological characteristics on the EIS signature. The characteristic impedance spectra of an electrochemical NMC half cell in Nyquist plot can be composed of two semicircles in high and mid frequency ranges followed by a sloping tail in low frequencies [1]. While the interfacial impedance contributes dominantly into the dynamic response in low and mid range of frequencies, the electrode-scale ionic and electronic impedances are minor in this range. At high frequencies, the faradaic contribution diminishes and therefore, the interfacial impedance exhibits mostly capacitive behavior, resulting in more dominance of the electrode-scale impedance (electronic and ionic) in the total impedance spectra. However, previous works reported a sloping line in high frequency range which deviates from the semicircle spectra. The origin of this deviation has been studied by Pouraghajan et al. [85] and it has been attributed to missing contact resistance between the electrode and the current collector. In the current study, since the main focus is on the effect of electrode microstructure on the impedance spectra, no such contact resistance is assumed in the developed model leading to sloping lines in the high frequency range, as depicted in the inset Nyquist plot in Figure 7a.

4.2.1. Effect of CBD Content on Impedance Spectra

Figure 7a presents the calculated impedance response of the developed half-cell by lithiation state of 50% with different CBD contents. As mentioned earlier, presence of CBD results in partial blockage of the AM-electrolyte interfaces. This provides a confined site leading to reduced electrochemical kinetics. The larger dimension of mid-frequency semicircle obtained by more CBD content is caused by the limited kinetics in the electrode.
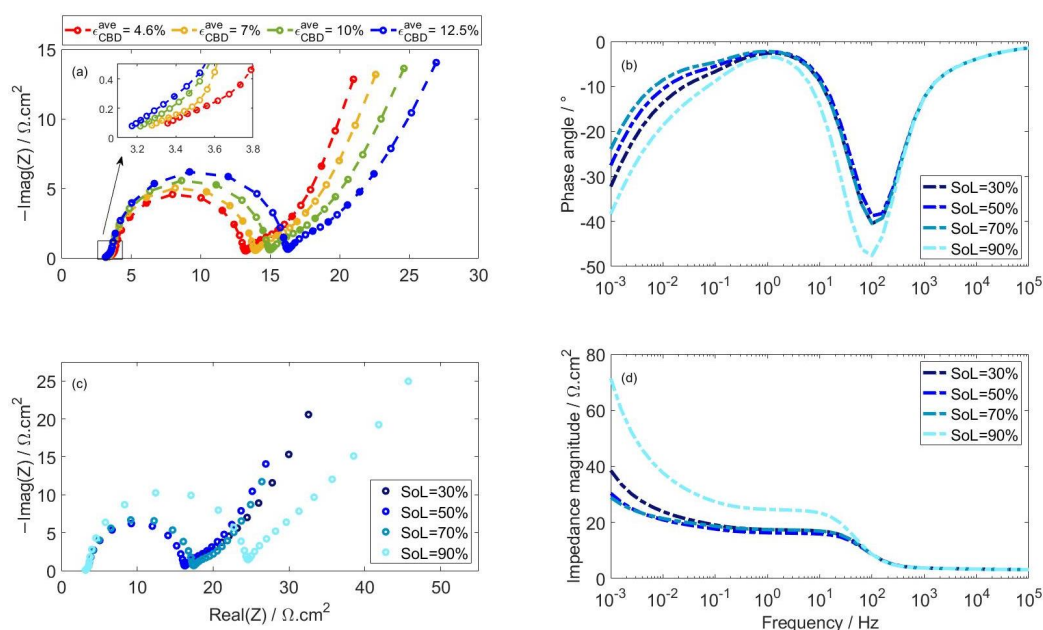
Figure 7. Nyquist plots of computed EIS for the half-cell by heterogeneous model for different CBD contents at 50% SoL (**a**) and phase angle (**b**), Nyquist plot (**c**) and impedance magnitude (**d**) of the half-cell for different SoLs for the same CBD content of 12.5%.

Simultaneously, the CBD content influences the transport limitations across the electrode as well. The high frequency inset Nyquist plot in Figure 7a shows slopes with varying angles which is in contrast to the constant 45° slope that is predicted by TLM in high-frequency impedance spectra. Such deviation has also been described for fractal, porous electrode structure with open and closed ends as well as packed spherical particles electrode by Cooper et al. [86]. The different slopes are attributed to the pore geometry of the microstructure. As illustrated in the inset Nyquist plot in Figure 7a, more content of CBD results in elevated angle of slope which can be attributed to narrower diffusive flux passage for the transport process. In other words, more CBD content provides a hindered diffusive flux characteristics leading to phase increase of the impedance in the high frequency range. This is in agreement with the conclusion which has been made by Cooper et al. on the impact of pore geometry on the impedance spectra. The deteriorated transport in pore domain by increasing CBD content is also aligned with the attained effective ionic transport coefficient shown in Figure 4c–f. The intersection of the impedance spectra with horizontal axis represents the electronic transport limitation of the half-cell. Higher overall effective electronic conductivity of the electrode with more CBD content, Figure 6c, results in shifting the intersection toward left that proves less transport limitation.

4.2.2. Effect of State of Lithiation on Impedance Spectra

Figure 7b–d demonstrate the evolution of the impedance response of the developed half-cell with different state of lithiations (SoLs) for a CBD content of 12.5%. The correlation of the faradaic reaction kinetics with the AM particles' surface SoL in the Butler–Volmer equation results in various kinetics limitations in diverse SoLs. In other words, high or low surface SoL results in low faradaic current density and increases the interfacial impedance while the electrode microstructure stays unchanged. This effect is shown by the Nyquist plot in Figure 7c and the larger dimension of mid frequency semicircle is due to more constrained kinetics in high or low lithiation states. This is further confirmed by the impedance phase and magnitude for different SoLs displayed in Figure 7b,d. The lithiation state affects the impedance only in the low frequency range where the interfacial impedance is dominant while the impedance in higher frequencies stays invariant. This is due to the

fact that at higher frequencies, interactions other than intercalation and deintercalaction reactions dominate the impedance spectra.

4.3. Modified Continuum Model

The continuum model is modified regarding parametrization and then compared to the heterogeneous model in terms of EIS response to enable high resolution comparison. For this purpose, the spatially resolved volumetric contents of the AM, pore and carbon-binder domains, provided in Figure 3a–c, are fed into the model as opposed to the commonly used average-based values in the unmodified model. Furthermore, the specific active surface area (Figure 3d), which strongly impacts the cell kinetics, is defined locally. Similarly, the calculated effective transport coefficients in pore and solid domains along the electrode thickness (Figures 4 and 6) are translated into the model, as opposed to the Bruggeman formulation.

The assigned particle size into the modified and unmodified continuum models is similar and defined based on the averaged particle size $\bar{r}_p$. It is important to point out this parameter is not the r_p introduced as average initial (spherical) particle radius being 5 μm or 2 μm. Even though the number-averaged size is often used for the P2D model, $\bar{r}_p$ is calculated as the volume-averaged radius in this study, since the larger particles show a slower kinetics of lithiation and delithiation and are significantly determining on the overall dynamic response of the electrode [4].

Although the electrode is still modeled in one dimension in the modified continuum model, the locally-resolved parameters assist to improve this modeling approach by including the microstructure effects within the electrode thickness. Figure 8 shows the Nyquist plots of the impedance spectra of the half-cell calculated by the modeling approaches for different CBD contents. In comparison to the heterogeneous model as the benchmark, the deviation of the mid frequency semicircle and sloping tail in the low frequency range computed by the unmodified continuum model increases as the CBD content in the electrode rises. In other words, more CBD content results in more deficiency of the conventionally parameterized continuum model to catch the complexities of the electrode morphology and the kinetics limitations arising from the microstructure. Figure 8 indicates the improved capabilty of the modified continuum model to predict restraints compared to the conventionally parameterized continuum model.

Figure 9 illustrates the calculated half-cell voltage during the discharge at 2C-rate based on different modeling approaches to provide a more comprehensive picture on the effectiveness of the introduced modified model. The discharge curve depicts the resemblance of the modified continuum model to the heterogeneous model output. The higher voltage drop predicted by the heterogeneous model compared to both modified and unmodified continuum models is mainly attributed to the size and shape irregularities of the AM particles. The concentration of lithium inside larger particles is more uneven and it reaches its maxima at the end of lithiation. Such heterogeneity results in generation of high overpotential (voltage drop) at the end of the discharge process. However, the inherent inadequacy of the continuum modeling approach which assumes the homogeneous spherical AM particles to be the same size leads to prediction of comparatively less uneven lithium concentration inside AM particles and therefore, the calculated voltage drop at the end of discharge process is underestimated compared to its counter value predicted by the heterogeneous model.
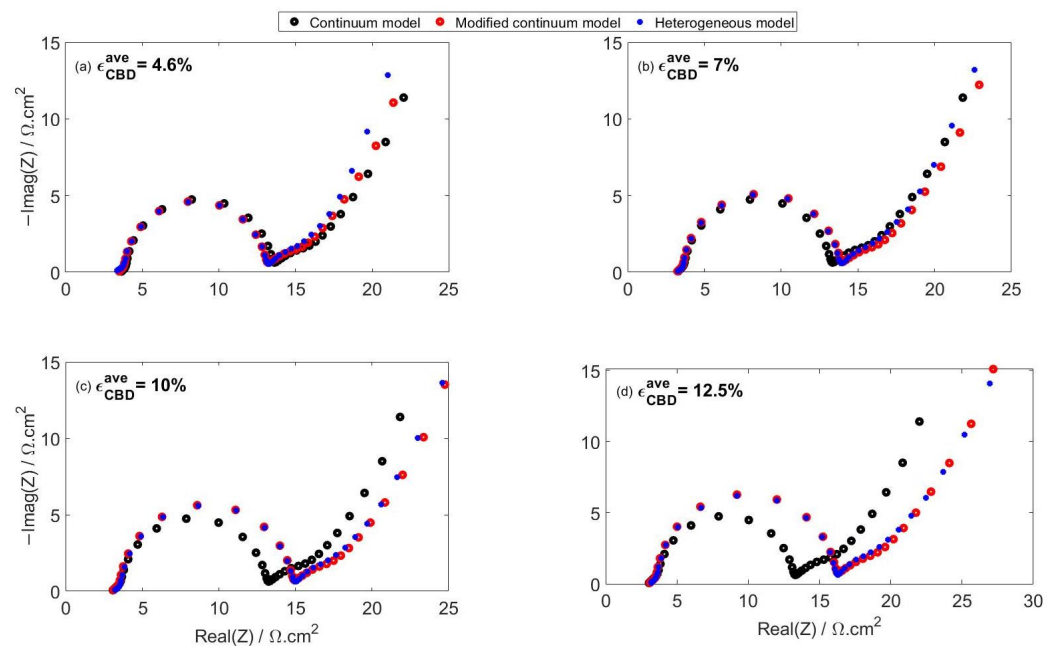
Figure 8. Nyquist plots of the impedance spectra of the half-cell calculated by different modeling approaches in diverse CBD contents.
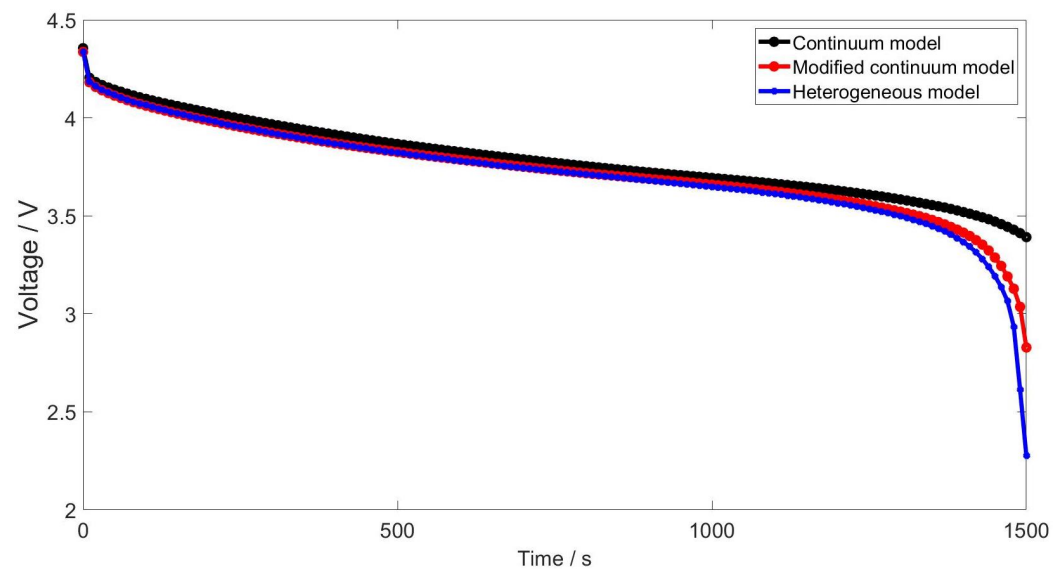
Figure 9. Half-cell discharge voltage at 2C-rate computed by different modeling approaches.

5. Conclusions

State-of-the-art porous electrodes are multiphase structures in which each phase has specific electrochemical properties and interactions with each other. Generating a digital morphology of the electrode microstructure, which encompasses the same heterogeneities that exist in real electrodes, and the application of FEM modeling can be of great benefit in understanding the electrode and cell characteristics. In this regard, the proposed method showed a computationally efficient way to resolve the morphological complexities of the electrode and its constituents, active material, pore/electrolyte and carbon-binder domains.

The developed model allows the geometrical and transport properties of the electrode to be characterized. The functionality of the obtained values is also realized in the modification of the continuum model in terms of the parametrization procedure. In this context, the spatially resolved transport properties of the pore and solid domains were fed into the continuum model, in contrast to the commonly used analytical average values,

to account for the effect of the electrode microstructure. It was found that the predictions of the modified continuum model were improved in both the frequency and time domains. However, due to the presence of size and shape irregularities that cannot be accounted for in the continuum approach, a voltage deviation from the heterogeneous model remains.

The effects of the Carbon-Binder Domain (CBD) content on the impedance of the electrode were investigated. It was found that higher CBD content results in larger dimension of the mid-frequency semicircle, which is due to the increased kinetics constraints. Different CBD contents also affect the angle of the sloping line of the impdeance spectra in high frequency range and the intersection with the horizontal axis due to the different ionic and electronic transport limitations. It was also observed that the state of lithiation affects the impedance spectra in the mid- and low-frequency range, where intercalation is the dominant contributor.

Author Contributions: Conceptualization, M.M. and B.V.; methodology, M.M. and B.V.; software, M.M. and B.V.; validation, M.M. and J.K.; formal analysis, M.M. and B.V.; investigation, M.M.; resources, S.P.; data curation, M.M.; writing—original draft preparation, M.M. and B.V.; writing—review and editing, J.K.; visualization, M.M. and B.V.; supervision, J.K.; project administration, S.P. All authors have read and agreed to the published version of the manuscript.

Data Availability Statement: Not applicable.

Abbreviations

Thefollowing abbreviations are used in this manuscript:

Latin Letters

A	Noise amplitude	[μm]	Section 2.1
A_v	Specific active surface area	[1/m]	Section 3.1
a	Randomly generated scalar parameter		Section 2.1
b	Randomly generated scalar parameter		Section 2.1
C_{DL}	Specific double layer capacitance	[F/m²]	Section 3.1
c_e	Electrolyte concentration	[mol/m³]	Section 3.1
c_s	Solid concentration	[mol/m³]	Section 3.1
$D_e^{\text{bulk}}, D_e^{\text{eff}}$	Bulk and effective electrolyte diffusivity	[m²/s]	Section 3.1
D_s	Solid diffusivity	[m²/s]	Section 3.1
d	Particle diameter	[μm]	Section 2.1
F	Faraday constant	[C/mol]	Section 3.1
j	Stream flux	[m/s]	Section 2.2
j_0	Exchange current density	[A/m²]	Section 3.1
j^f	Volumetric faradaic current	[A/m³]	Section 3.1
j^c	Volumetric capacitive current	[A/m³]	Section 3.1
k	Reaction rate constant	[m/s]	Section 3.1
L	RVE length	[μm]	Section 2.1
N	Normal distribution		Section 2.1
P	Associated Legendre polynomial		Section 2.1
R	Gas constant	[J/mol·K]	Section 3.1
r	Radius	[μm]	Section 2.1
r_p	Average particle radius	[μm]	Section 2.1
$\bar{r}_p$	Volume average radius	[μm]	Section 4.3
S	Sphere/circle		Section 2.1
T	Temperature	[K]	Section 3.1
U	Open circuit voltage	[V]	Section 3.1
Y	Spherical harmonics function		Section 2.1
Z	Random variable		Section 2.1

Greek Letters

α_a, α_c	Symmetry coefficient		Section 3.1
$\alpha_{\mathrm{bulk}}, \alpha_{\mathrm{eff}}$	Bulk and effective transport coefficients	[m²/s]	Section 2.2
ε	Volumetric fraction		Section 2.2
Γ	Spatial 3D domain		Section 2.2
φ	Azimuth angle of a sphere	[°]	Section 2.1
ϕ	Dimensionless potential field		Section 2.2
$\overline{\phi}$	Averaged dimensionless potential field		Section 2.2
ϕ_e	Electrolyte electrochemical potential	[V]	Section 3.1
ϕ_s	Solid electrical potential	[V]	Section 3.1
ρ	Radius of generated irregular particle	[μm]	Section 2.1
σ	Standard deviation		Section 2.1
$\kappa_e^{\mathrm{bulk}}, \kappa_e^{\mathrm{eff}}$	Bulk and effective electrolyte conductivity	[S/m]	Section 3.1
$\sigma_s^{\mathrm{bulk}}, \sigma_s^{\mathrm{eff}}$	Bulk and effective solid conductivity	[S/m]	Section 3.1
η	Overpotential	[V]	Section 3.1
μ	Mean of distribution		Section 2.1
τ	Tortusity factor		Section 2.2
θ	Polar angle of a sphere	[°]	Section 2.1
Υ	Surface of irregular spherical shape		Section 2.1

Abbreviations

AM	Active Material
CBD	Carbon Binder Domain
CC	Current Collector
DL	Double layer
EIS	Electrochemical Impedance Spectroscopy
FIB	Focused Ion Beam
HC	Spherical Harmonic Coefficients
N_M	MacMullin number
PDE	Partial Differential Equation
SEM	Scanning Electron Microscopy
SoL	State of Lithiation
TEM	Transmission Electron Microscopy
XCT	X-ray Computed Tomography

Subscripts

l, m	Legendre polynomial and spherical harmonics, degree, order
s, e	Solid, electrolyte

References

1. Ansah, S.; Hyun, H.; Shin, N.; Lee, J.S.; Lim, J.; Cho, H.H. A modeling approach to study the performance of Ni-rich layered oxide cathode for lithium-ion battery. *Comput. Mater. Sci.* **2021**, *196*, 110559. [CrossRef]
2. Doyle, M.; Fuller, T.F.; Newman, J. Modeling of Galvanostatic Charge and Discharge of the Lithium/Polymer/Insertion Cell. *J. Electrochem. Soc.* **1993**, *140*, 1526–1533. [CrossRef]
3. Fuller, T.F.; Doyle, M.; Newman, J. Simulation and Optimization of the Dual Lithium Ion Insertion Cell. *J. Electrochem. Soc.* **1994**, *141*, 1–10. [CrossRef]
4. Fang, R.; Ge, H.; Wang, Z.; Li, Z.; Zhang, J. A Two-Dimensional Heterogeneous Model of Lithium-Ion Battery and Application on Designing Electrode with Non-Uniform Porosity. *J. Electrochem. Soc.* **2020**, *167*, 130513. [CrossRef]
5. Tjaden, B.; Cooper, S.J.; Brett, D.J.; Kramer, D.; Shearing, P.R. On the origin and application of the Bruggeman correlation for analysing transport phenomena in electrochemical systems. *Curr. Opin. Chem. Eng.* **2016**, *12*, 44–51. [CrossRef]
6. García, R.E.; Chiang, Y.M.; Carter, W.C.; Limthongkul, P.; Bishop, C.M. Microstructural modeling and design of rechargeable lithium-ion batteries. *J. Electrochem. Soc.* **2004**, *152*, A255. [CrossRef]
7. Liu, P.; Xu, R.; Liu, Y.; Lin, F.; Zhao, K. Computational modeling of heterogeneity of stress, charge, and cyclic damage in composite electrodes of Li-ion batteries. *J. Electrochem. Soc.* **2020**, *167*, 40527. [CrossRef]
8. Mistry, A.N.; Smith, K.; Mukherjee, P.P. Secondary-phase stochastics in lithium-ion battery electrodes. *ACS Appl. Mater. Interfaces* **2018**, *10*, 6317–6326. [CrossRef]
9. Latham, J.P.; Munjiza, A. The modelling of particle systems with real shapes. *Philos. Trans. R. Soc. Lon. Ser. A Math. Phys. Eng. Sci.* **2004**, *362*, 1953–1972. [CrossRef]

10. Yang, Y.; Xu, R.; Zhang, K.; Lee, S.J.; Mu, L.; Liu, P.; Waters, C.K.; Spence, S.; Xu, Z.; Wei, C.; et al. Quantification of Heterogeneous Degradation in Li–Ion Batteries. *Adv. Energy Mater.* **2019**, *9*, 1900674. [CrossRef]

11. Kashkooli, A.G.; Amirfazli, A.; Farhad, S.; Lee, D.U.; Felicelli, S.; Park, H.W.; Feng, K.; De Andrade, V.; Chen, Z. Representative volume element model of lithium-ion battery electrodes based on X-ray nano-tomography. *J. Appl. Electrochem.* **2017**, *47*, 281–293. [CrossRef]

12. Cooper, S.J.; Eastwood, D.S.; Gelb, J.; Damblanc, G.; Brett, D.; Bradley, R.S.; Withers, P.J.; Lee, P.D.; Marquis, A.J.; Brandon, N.P.; et al. Image based modelling of microstructural heterogeneity in LiFePO$_4$ electrodes for Li-ion batteries. *J. Power Sources* **2014**, *247*, 1033–1039. [CrossRef]

13. Danner, T.; Singh, M.; Hein, S.; Kaiser, J.; Hahn, H.; Latz, A. Thick electrodes for Li-ion batteries: A model based analysis. *J. Power Sources* **2016**, *334*, 191–201. [CrossRef]

14. Stephenson, D.E.; Walker, B.C.; Skelton, C.B.; Gorzkowski, E.P.; Rowenhorst, D.J.; Wheeler, D.R. Modeling 3D microstructure and ion transport in porous Li-ion battery electrodes. *J. Electrochem. Soc.* **2011**, *158*, A781. [CrossRef]

15. Heenan, T.M.M.; Jnawali, A.; Kok, M.D.R.; Tranter, T.G.; Tan, C.; Dimitrijevic, A.; Jervis, R.; Brett, D.J.L.; Shearing, P.R. An Advanced Microstructural and Electrochemical Datasheet on 18650 Li-Ion Batteries with Nickel-Rich NMC811 Cathodes and Graphite-Silicon Anodes. *J. Electrochem. Soc.* **2020**, *167*, 140530. [CrossRef]

16. Hein, S.; Danner, T.; Westhoff, D.; Prifling, B.; Scurtu, R.; Kremer, L.; Hoffmann, A.; Hilger, A.; Osenberg, M.; Manke, I.; et al. Influence of Conductive Additives and Binder on the Impedance of Lithium-Ion Battery Electrodes: Effect of Morphology. *J. Electrochem. Soc.* **2020**, *167*, 013546. [CrossRef]

17. Jiang, Z.; Li, J.; Yang, Y.; Mu, L.; Wei, C.; Yu, X.; Pianetta, P.; Zhao, K.; Cloetens, P.; Lin, F.; et al. Machine-learning-revealed statistics of the particle-carbon/binder detachment in lithium-ion battery cathodes. *Nat. Commun.* **2020**, *11*, 2310. [CrossRef]

18. Lu, X.; Bertei, A.; Finegan, D.P.; Tan, C.; Daemi, S.R.; Weaving, J.S.; O'Regan, K.B.; Heenan, T.M.M.; Hinds, G.; Kendrick, E.; et al. 3D microstructure design of lithium-ion battery electrodes assisted by X-ray nano-computed tomography and modelling. *Nat. Commun.* **2020**, *11*, 2079. [CrossRef]

19. Mayer, J.K.; Almar, L.; Asylbekov, E.; Haselrieder, W.; Kwade, A.; Weber, A.; Nirschl, H. Influence of the Carbon Black Dispersing Process on the Microstructure and Performance of Li-Ion Battery Cathodes. *Energy Technol.* **2020**, *8*, 1900161. [CrossRef]

20. Terreblanche, J.; Thompson, D.; Aldous, I.; Hartley, J.; Abbott, A.; Ryder, K.S. Experimental visualization of commercial lithium ion battery cathodes: Distinguishing between the microstructure components using atomic force microscopy. *J. Phys. Chem. C* **2020**, *124*, 14622–14631. [CrossRef]

21. Xu, R.; Yang, Y.; Yin, F.; Liu, P.; Cloetens, P.; Liu, Y.; Lin, F.; Zhao, K. Heterogeneous damage in Li-ion batteries: Experimental analysis and theoretical modeling. *J. Mech. Phys. Solids* **2019**, *129*, 160–183. [CrossRef]

22. Ngandjong, A.C.; Rucci, A.; Maiza, M.; Shukla, G.; Vazquez-Arenas, J.; Franco, A.A. Multiscale simulation platform linking lithium ion battery electrode fabrication process with performance at the cell level. *J. Phys. Chem. Lett.* **2017**, *8*, 5966–5972. [CrossRef] [PubMed]

23. Feinauer, J.; Westhoff, D.; Kuchler, K.; Schmidt, V. 3D Microstructure Modeling and Simulation of Materials in Lithium-ion Battery Cells. In *Proceedings of the Simulation Science*; Springer: Cham, Switzerland, 2018; pp. 128–144. .{_}8. [CrossRef]

24. Furat, O.; Petrich, L.; Finegan, D.P.; Diercks, D.; Usseglio-Viretta, F.; Smith, K.; Schmidt, V. Artificial generation of representative single Li-ion electrode particle architectures from microscopy data. *npj Comput. Mater.* **2021**, *7*, 105. [CrossRef]

25. Mai, W.; Yang, M.; Soghrati, S. A particle-resolved 3D finite element model to study the effect of cathode microstructure on the behavior of lithium ion batteries. *Electrochim. Acta* **2019**, *294*, 192–209. [CrossRef]

26. Bistri, D.; Afshar, A.; Di Leo, C.V. Modeling the chemo-mechanical behavior of all-solid-state batteries: A review. *Meccanica* **2021**, *56*, 1523–1554. [CrossRef]

27. Forouzan, M.M.; Chao, C.W.; Bustamante, D.; Mazzeo, B.A.; Wheeler, D.R. Experiment and simulation of the fabrication process of lithium-ion battery cathodes for determining microstructure and mechanical properties. *J. Power Sources* **2016**, *312*, 172–183. [CrossRef]

28. Awarke, A.; Wittler, M.; Pischinger, S.; Bockstette, J. A 3D Mesoscale Model of the Collector-Electrode Interface in Li-Ion Batteries. *J. Electrochem. Soc.* **2012**, *159*, A798–A808. [CrossRef]

29. Oehler, D.; Seegert, P.; Wetzel, T. Modeling the Thermal Conductivity of Porous Electrodes of Li-Ion Batteries as a Function of Microstructure Parameters. *Energy Technol.* **2021**, *9*, 2000574. [CrossRef]

30. Santoki, J.; Daubner, S.; Schneider, D.; Kamlah, M.; Nestler, B. Effect of tortuosity, porosity, and particle size on phase-separation dynamics of ellipsoid-like particles of porous electrodes: Cahn–Hilliard-type phase-field simulations. *Model. Simul. Mater. Sci. Eng.* **2021**, *29*, 065010. [CrossRef]

31. Xu, H.; Bae, C. Stochastic 3D microstructure reconstruction and mechanical modeling of anisotropic battery separators. *J. Power Sources* **2019**, *430*, 67–73. [CrossRef]

32. Tu, V. Modeling and Finite Element Simulation of the Bifunctional Performance of a Microporous Structural Battery Electrolyte. Master's Thesis, Chalmers University of Technology, Gothenburg, Sweden, 2019.

33. Nguyen, T.T.; Demortière, A.; Fleutot, B.; Delobel, B.; Delacourt, C.; Cooper, S.J. The electrode tortuosity factor: Why the conventional tortuosity factor is not well suited for quantifying transport in porous Li-ion battery electrodes and what to use instead. *npj Comput. Mater.* **2020**, *6*, 123. [CrossRef]

34. Allen, J.M.; Chang, J.; Usseglio-Viretta, F.L.E.; Graf, P.; Smith, K. A Segregated Approach for Modeling the Electrochemistry in the 3-D Microstructure of Li-Ion Batteries and Its Acceleration Using Block Preconditioners. *J. Sci. Comput.* **2021**, *86*, 42. [CrossRef]

35. He, X.; Bresser, D.; Passerini, S.; Baakes, F.; Krewer, U.; Lopez, J.; Mallia, C.T.; Shao-Horn, Y.; Cekic-Laskovic, I.; Wiemers-Meyer, S.; et al. The passivity of lithium electrodes in liquid electrolytes for secondary batteries. *Nat. Rev. Mater.* **2021**, *6*, 1036–1052. [CrossRef]

36. An, F.; Zhou, W.; Li, P. A comparison of model prediction from P2D and particle packing with experiment. *Electrochim. Acta* **2021**, *370*, 137775. [CrossRef]

37. Chouchane, M.; Rucci, A.; Lombardo, T.; Ngandjong, A.C.; Franco, A.A. Lithium ion battery electrodes predicted from manufacturing simulations: Assessing the impact of the carbon-binder spatial location on the electrochemical performance. *J. Power Sources* **2019**, *444*, 227285. [CrossRef]

38. Renganathan, S.; Sikha, G.; Santhanagopalan, S.; White, R.E. Theoretical analysis of stresses in a lithium ion cell. *J. Electrochem. Soc.* **2009**, *157*, A155. [CrossRef]

39. Cheng, Y.T.; Verbrugge, M.W. Evolution of stress within a spherical insertion electrode particle under potentiostatic and galvanostatic operation. *J. Power Sources* **2009**, *190*, 453–460. [CrossRef]

40. Gao, X.; Lu, W.; Xu, J. Modeling framework for multiphysics-multiscale behavior of Si–C composite anode. *J. Power Sources* **2020**, *449*, 227501. [CrossRef]

41. Liu, B.; Jia, Y.; Li, J.; Jiang, H.; Yin, S.; Xu, J. Multiphysics coupled computational model for commercialized Si/graphite composite anode. *J. Power Sources* **2020**, *450*, 227667. [CrossRef]

42. Wang, M.; Xiao, X.; Huang, X. A multiphysics microstructure-resolved model for silicon anode lithium-ion batteries. *J. Power Sources* **2017**, *348*, 66–79. [CrossRef]

43. Wu, W.; Xiao, X.; Wang, M.; Huang, X. A microstructural resolved model for the stress analysis of lithium-ion batteries. *J. Electrochem. Soc.* **2014**, *161*, A803. [CrossRef]

44. Ahmadi, M. A hybrid phase field model for fracture induced by lithium diffusion in electrode particles of Li-ion batteries. *Comput. Mater. Sci.* **2020**, *184*, 109879. [CrossRef]

45. Lee, S.; Yang, J.; Lu, W. Debonding at the interface between active particles and PVDF binder in Li-ion batteries. *Extrem. Mech. Lett.* **2016**, *6*, 37–44. [CrossRef]

46. Grantab, R.; Shenoy, V.B. Pressure-gradient dependent diffusion and crack propagation in lithiated silicon nanowires. *J. Electrochem. Soc.* **2012**, *159*, A584. [CrossRef]

47. Stein, M.; Mistry, A.; Mukherjee, P.P. Mechanistic understanding of the role of evaporation in electrode processing. *J. Electrochem. Soc.* **2017**, *164*, A1616. [CrossRef]

48. Font, F.; Protas, B.; Richardson, G.; Foster, J.M. Binder migration during drying of lithium-ion battery electrodes: Modelling and comparison to experiment. *J. Power Sources* **2018**, *393*, 177–185. [CrossRef]

49. Ngandjong, A.C.; Lombardo, T.; Primo, E.N.; Chouchane, M.; Shodiev, A.; Arcelus, O.; Franco, A.A. Investigating electrode calendering and its impact on electrochemical performance by means of a new discrete element method model: Towards a digital twin of Li-Ion battery manufacturing. *J. Power Sources* **2021**, *485*, 229320. [CrossRef]

50. Mirsalehian, M.; Vossoughi, B.; Kaiser, J.; Pischinger, S. 2022, *in preparation*.

51. Varshalovich, D.A.; Moskalev, A.N.; Khersonskii, V.K. *Quantum Theory of Angular Momentum*; World Scientific: Singapore, 1988.

52. Claessens, S.J. Spherical harmonic analysis of a harmonic function given on a spheroid. *Geophys. J. Int.* **2016**, *206*, 142–151. [CrossRef]

53. Barthelmes, F. Definition of Functionals of the Geopotential and Their Calculation from Spherical Harmonic Models: Theory and Formulas Used by the Calculation Service of the International Centre for Global Earth Models (ICGEM). 2009. Available online: http://icgem.gfz-potsdam.de/str-0902-revised.pdf (accessed on 26 May 2023). [CrossRef]

54. Granzow, K.D. Spherical harmonic representation of the magnetic field in the presence of a current density. *Geophys. J. Int.* **1983**, *74*, 489–505. [CrossRef]

55. Balmino, G.; Vales, N.; Bonvalot, S.; Briais, A. Spherical harmonic modelling to ultra-high degree of Bouguer and isostatic anomalies. *J. Geod.* **2012**, *86*, 499–520. [CrossRef]

56. Tsoulis, D. *Spherical Harmonic Computations with Topographic/Isostatic Coefficients*; Technical Report; Institut für Astronomische und Physikalische Geodäsie, Technical University Munich: Munich, Germany, 1999.

57. Amirbekyan, A.; Michel, V.; Simons, F.J. Parametrizing surface wave tomographic models with harmonic spherical splines. *Geophys. J. Int.* **2008**, *174*, 617–628. [CrossRef]

58. Parimal, S.; Cramer, S.M.; Garde, S. Application of a spherical harmonics expansion approach for calculating ligand density distributions around proteins. *J. Phys. Chem. B* **2014**, *118*, 13066–13076. [CrossRef] [PubMed]

59. Medyukhina, A.; Blickensdorf, M.; Cseresnyés, Z.; Ruef, N.; Stein, J.V.; Figge, M.T. Dynamic spherical harmonics approach for shape classification of migrating cells. *Sci. Rep.* **2020**, *10*, 6072. [CrossRef] [PubMed]

60. Ge, W. *High-Order Spherical Harmonics Methods for Radiative Heat Transfer and Applications in Combustion Simulations*; University of California: Merced, CA, USA, 2017.

61. Tapimo, R.; Kamdem, H.T.T. A spherical harmonic formulation for radiative heat transfer analysis. *Am. J. Heat Mass Transf.* **2016**, *3*, 280–295. [CrossRef]

62. Wang, X.; Yin, Z.Y.; Xiong, H.; Su, D.; Feng, Y.T. A spherical-harmonic-based approach to discrete element modeling of 3D irregular particles. *Int. J. Numer. Methods Eng.* **2021**, *122*, 5626–5655. [CrossRef]

63. Feinauer, J.; Spettl, A.; Manke, I.; Strege, S.; Kwade, A.; Pott, A.; Schmidt, V. Structural characterization of particle systems using spherical harmonics. *Mater. Charact.* **2015**, *106*, 123–133. [CrossRef]

64. Liu, X.; Garboczi, E.; Grigoriu, M.; Lu, Y.; Erdoğan, S.T. Spherical harmonic-based random fields based on real particle 3D data: Improved numerical algorithm and quantitative comparison to real particles. *Powder Technol.* **2011**, *207*, 78–86. [CrossRef]

65. Westhoff, D.; Feinauer, J.; Kuchler, K.; Mitsch, T.; Manke, I.; Hein, S.; Latz, A.; Schmidt, V. Parametric stochastic 3D model for the microstructure of anodes in lithium-ion power cells. *Comput. Mater. Sci.* **2017**, *126*, 453–467. [CrossRef]

66. Feinauer, J.; Brereton, T.; Spettl, A.; Weber, M.; Manke, I.; Schmidt, V. Stochastic 3D modeling of the microstructure of lithium-ion battery anodes via Gaussian random fields on the sphere. *Comput. Mater. Sci.* **2015**, *109*, 137–146. [CrossRef]

67. Westhoff, D.; Manke, I.; Schmidt, V. Generation of virtual lithium-ion battery electrode microstructures based on spatial stochastic modeling. *Comput. Mater. Sci.* **2018**, *151*, 53–64. [CrossRef]

68. Kuchler, K.; Westhoff, D.; Feinauer, J.; Mitsch, T.; Manke, I.; Schmidt, V. Stochastic model for the 3D microstructure of pristine and cyclically aged cathodes in Li-ion batteries. *Model. Simul. Mater. Sci. Eng.* **2018**, *26*, 035005. [CrossRef]

69. Griffiths, D. *Introduction to Quantum Mechanics*; Pearson: Upper Saddle River, NJ, USA, 2006.

70. Chen, Y.H.; Wang, C.W.; Liu, G.; Song, X.Y.; Battaglia, V.; Sastry, A.M. Selection of conductive additives in li-ion battery cathodes: A numerical study. *J. Electrochem. Soc.* **2007**, *154*, A978. [CrossRef]

71. Sturm, J.; Rheinfeld, A.; Zilberman, I.; Spingler, F.B.; Kosch, S.; Frie, F.; Jossen, A. Modeling and simulation of inhomogeneities in a 18650 nickel-rich, silicon-graphite lithium-ion cell during fast charging. *J. Power Sources* **2019**, *412*, 204–223. [CrossRef]

72. Ko, J.Y.; Varini, M.; Klett, M.; Ekström, H.; Lindbergh, G. Porous Electrode Model with Particle Stress Effects for Li (Ni1/3Co1/3Mn1/3) O2 Electrode. *J. Electrochem. Soc.* **2019**, *166*, A2939. [CrossRef]

73. Zheng, W.; Shui, M.; Shu, J.; Gao, S.; Xu, D.; Chen, L.; Feng, L.; Ren, Y. GITT studies on oxide cathode LiNi1/3Co1/3Mn1/3O2 synthesized by citric acid assisted high-energy ball milling. *Bull. Mater. Sci.* **2013**, *36*, 495–498. [CrossRef]

74. Mistry, A.N.; Mukherjee, P.P. Probing spatial coupling of resistive modes in porous intercalation electrodes through impedance spectroscopy. *Phys. Chem. Chem. Phys.* **2019**, *21*, 3805–3813. [CrossRef]

75. Zavalis, T.G.; Behm, M.; Lindbergh, G. Investigation of short-circuit scenarios in a lithium-ion battery cell. *J. Electrochem. Soc.* **2012**, *159*, A848. [CrossRef]

76. Nyman, A.; Behm, M.; Lindbergh, G. Electrochemical characterisation and modelling of the mass transport phenomena in LiPF6–EC–EMC electrolyte. *Electrochim. Acta* **2008**, *53*, 6356–6365. [CrossRef]

77. Keiser, H.; Beccu, K.; Gutjahr, M. Abschätzung der porenstruktur poröser elektroden aus impedanzmessungen. *Electrochim. Acta* **1976**, *21*, 539–543. [CrossRef]

78. Itagaki, M.; Hatada, Y.; Shitanda, I.; Watanabe, K. Complex impedance spectra of porous electrode with fractal structure. *Electrochim. Acta* **2010**, *22*, 1229. [CrossRef]

79. Kant, R.; Singh, M.B. Theory of the Electrochemical Impedance of Mesostructured Electrodes Embedded with Heterogeneous Micropores. *J. Phys. Chem. C* **2017**, *121*, 7164–7174. [CrossRef]

80. Landesfeind, J.; Hattendorff, J.; Ehrl, A.; Wall, W.A.; Gasteiger, H.A. Tortuosity determination of battery electrodes and separators by impedance spectroscopy. *J. Electrochem. Soc.* **2016**, *163*, A1373. [CrossRef]

81. Shodiev, A.; Primo, E.N.; Chouchane, M.; Lombardo, T.; Ngandjong, A.C.; Rucci, A.; Franco, A.A. 4D-resolved physical model for electrochemical impedance spectroscopy of Li (Ni1-x-yMnxCoy) O2-based cathodes in symmetric cells: Consequences in tortuosity calculations. *J. Power Sources* **2020**, *454*, 227871. [CrossRef]

82. Shodiev, A.; Chouchane, M.; Gaberscek, M.; Arcelus, O.; Xu, J.; Oularbi, H.; Yu, J.; Li, J.; Morcrette, M.; Franco, A.A. Deconvoluting the benefits of porosity distribution in layered electrodes on the electrochemical performance of Li-ion batteries. *Energy Storage Mater.* **2022**, *47*, 462–471. [CrossRef]

83. Planella, F.B.; Ai, W.; Boyce, A.; Ghosh, A.; Korotkin, I.; Sahu, S.; Sulzer, V.; Timms, R.; Tranter, T.; Zyskin, M.; et al. A continuum of physics-based lithium-ion battery models reviewed. *Prog. Energy* **2022**, *4*, 042003. [CrossRef]

84. Landesfeind, J.; Ebner, M.; Eldiven, A.; Wood, V.; Gasteiger, H.A. Tortuosity of battery electrodes: Validation of impedance-derived values and critical comparison with 3D tomography. *J. Electrochem. Soc.* **2018**, *165*, A469. [CrossRef]

85. Pouraghajan, F.; Knight, H.; Wray, M.; Mazzeo, B.; Subbaraman, R.; Christensen, J.; Wheeler, D. Quantifying tortuosity of porous Li-ion battery electrodes: Comparing polarization-interrupt and blocking-electrolyte methods. *J. Electrochem. Soc.* **2018**, *165*, A2644–A2653. [CrossRef]

86. Cooper, S.J.; Bertei, A.; Finegan, D.P.; Brandon, N.P. Simulated impedance of diffusion in porous media. *Electrochim. Acta* **2017**, *251*, 681–689. [CrossRef]